LETTER

doi:10.1038/nature18955

A partially differentiated interior for (1) Ceres deduced from its gravity field and shape

R. S. Park[1], A. S. Konopliv[1], B. G. Bills[1], N. Rambaux[2], J. C. Castillo-Rogez[1], C. A. Raymond[1], A. T. Vaughan[1], A. I. Ermakov[3], M. T. Zuber[3], R. R. Fu[4], M. J. Toplis[5], C. T. Russell[6], A. Nathues[7] & F. Preusker[8]

Remote observations of the asteroid (1) Ceres from ground- and space-based telescopes have provided its approximate density and shape, leading to a range of models for the interior of Ceres, from homogeneous to fully differentiated[1–6]. A previously missing parameter that can place a strong constraint on the interior of Ceres is its moment of inertia, which requires the measurement of its gravitational variation[1,7] together with either precession rate[8,9] or a validated assumption of hydrostatic equilibrium[10]. However, Earth-based remote observations cannot measure gravity variations and the magnitude of the precession rate is too small to be detected[9]. Here we report gravity and shape measurements of Ceres obtained from the Dawn spacecraft, showing that it is in hydrostatic equilibrium with its inferred normalized mean moment of inertia of 0.37. These data show that Ceres is a partially differentiated body, with a rocky core overlaid by a volatile-rich shell, as predicted in some studies[1,4,6]. Furthermore, we show that the gravity signal is strongly suppressed compared to that predicted by the topographic variation. This indicates that Ceres is isostatically compensated[11], such that topographic highs are supported by displacement of a denser interior. In contrast to the asteroid (4) Vesta[8,12], this strong compensation points to the presence of a lower-viscosity layer at depth, probably reflecting a thermal rather than compositional gradient[1,4]. To further investigate the interior structure, we assume a two-layer model for the interior of Ceres with a core density of 2,460–2,900 kilograms per cubic metre (that is, composed of CI and CM chondrites[13]), which yields an outer-shell thickness of 70–190 kilometres. The density of this outer shell is 1,680–1,950 kilograms per cubic metre, indicating a mixture of volatiles and denser materials such as silicates and salts[14]. Although the gravity and shape data confirm that the interior of Ceres evolved thermally[1,4,6], its partially differentiated interior indicates an evolution more complex than has been envisioned for mid-sized (less than 1,000 kilometres across) ice-rich rocky bodies.

The tri-axial shape of Ceres has been determined from Dawn[15] spacecraft images obtained during the 1,480-km High Altitude Mapping Orbit campaign, which acquired global coverage of Ceres' surface with a resolution of about 140 m. These images have been processed along with radiometric tracking data to obtain a three-dimensional shape model of Ceres via stereo reconstruction techniques[16,17]. The resulting volume of Ceres is $(434.0 \pm 1.5) \times 10^6\,\mathrm{km}^3$ with a volumetric mean radius of $R \approx 470$ km. The best-fitting ellipsoidal model of the global shape yields the principal semi-axes of $a_e = 483.1 \pm 0.2$ km, $b_e = 481.0 \pm 0.2$ km and $c_e = 445.9 \pm 0.2$ km, which gives a polar flattening of 0.075 ± 0.001. The main reason for the 2-km difference in principal semi-axes a_e and b_e is the high topography seen around 47° E and 227° E (Fig. 1a).

The radial offset of the centre of figure with respect to the centre of mass of Ceres is a first-order measure of the degree of internal homogeneity[8]. This offset is about 1.0 ± 0.3 km, indicating that there may be a small level of internal heterogeneity at the longest wavelength, such as variations in the outer-shell density or thickness, or an offset in the core location. All terrestrial Solar System bodies for which detailed topography is known have centre-of-mass to centre-of-figure offsets in the ~0–3-km range[8,12]. Considering that the offset for Ceres is broadly towards the high-topography region, it suggests a global-scale variation

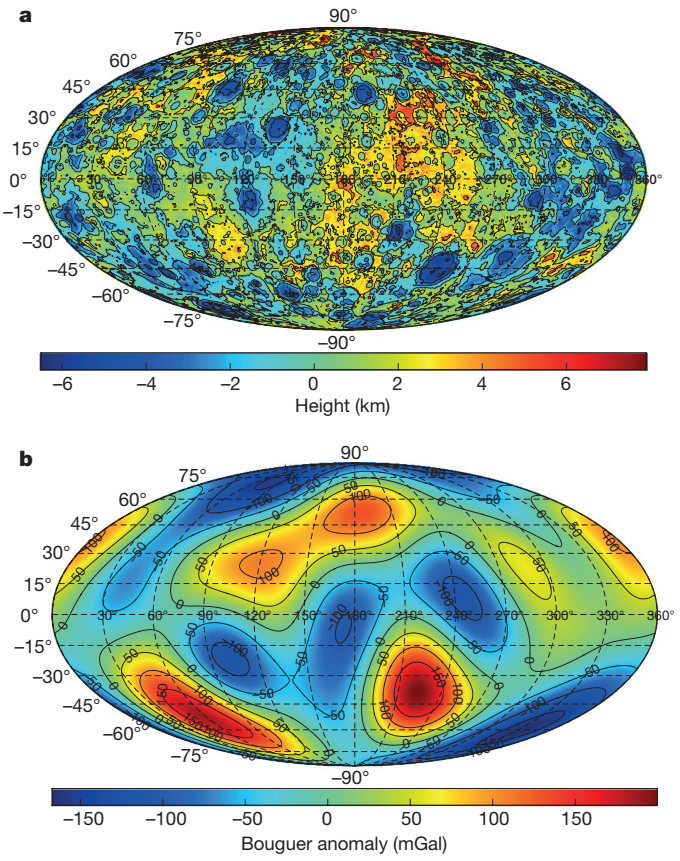

Figure 1 | Mollweide projection of topography and the Bouguer anomaly. a, Ceres topography map (ranging from −6.5 km to 7.9 km, colour scale). **b**, Bouguer anomaly map (ranging from −167 mGal to 200 mGal, colour scale and numbers on contours). Both maps are projected onto a (482 km, 482 km, 446 km) mean ellipsoid (see Methods). Projecting onto a geoid does not change the overall trends. Comparing both maps reveals a signature of a classic isostatic compensation of surface topography; that is, the Bouguer anomaly is inversely correlated with topography. This relation points to a decrease of viscosity at depth, probably caused by internal thermal gradients[1,4].

[1]Jet Propulsion Laboratory, California Institute of Technology, Pasadena, California 91109, USA. [2]IMCCE, Observatoire de Paris—PSL Research University, Sorbonne Universités—UPMC Université Paris 06, Université Lille 1, CNRS, 77 avenue Denfert-Rochereau, 75014 Paris, France. [3]Department of Earth, Atmospheric and Planetary Sciences, Massachusetts Institute of Technology, Cambridge, Massachusetts 02139, USA. [4]Lamont-Doherty Earth Observatory, Columbia University, Palisades, New York 10964, USA. [5]Institut de Recherche en Astrophysique et Planetologie, Université de Toulouse, CNRS, UPS, Toulouse, France. [6]Institute of Geophysics and Planetary Physics, University of California, Los Angeles, California 90095-1567, USA. [7]Max Planck Institute for Solar System Research, Goettingen, Germany. [8]Institute of Planetary Research, DLR, Department of Planetary Geodesy, Rutherfordstrasse 2, 12489 Berlin, Germany.

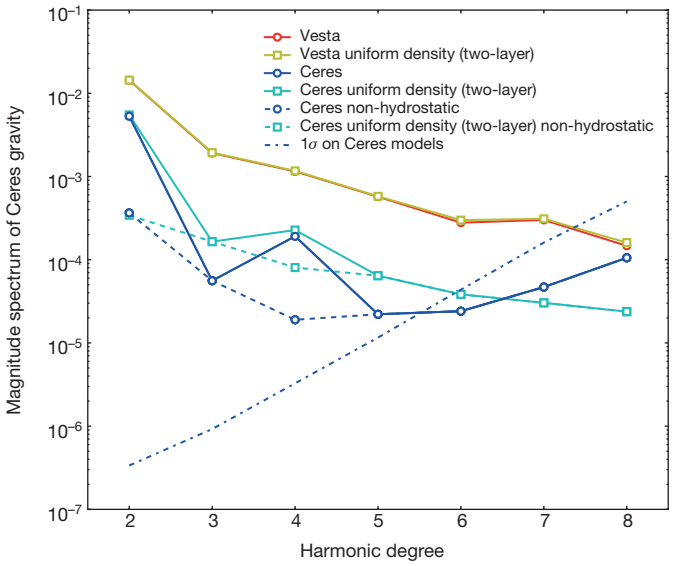

Figure 2 | Ceres gravity and error magnitude spectra of normalized spherical harmonic coefficients[7,8]. The observed Ceres gravity field (blue) shows a much lower signal than do uniform-density two-layer models (cyan). This becomes more apparent when the hydrostatic component is removed (dashed lines), showing that the gravity of Ceres is strongly suppressed, probably owing to isostatic compensation. The uniform-density Ceres gravity is based on a two-layer model with a 280-km spherical core with a constant 2,900 kg m^{-3} density (that is, CM-class chondrites[13]) and a constant outer-shell density of 1,950 kg m^{-3}. In contrast, the gravity field of Vesta (red) is mostly driven by the topographic signature of the surface (yellow)[8]. The Ceres gravity field is well determined for coefficients up to degree 5 (that is, the magnitude spectrum of uncertainty is lower than the estimated magnitude spectrum).

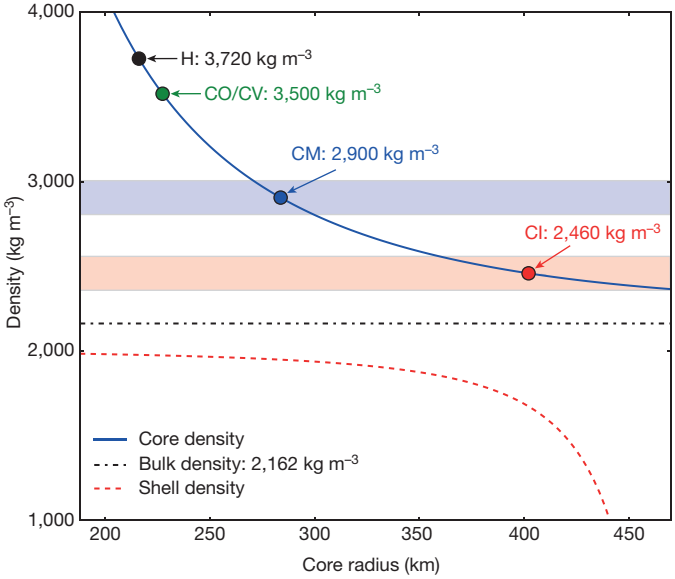

Figure 3 | Ceres core and shell densities computed by numerical integration of Clairaut's equations of hydrostatic equilibrium[9]. The core density values (solid blue line) and the shell density values (dashed red line) comprise the family of possible two-layer models for Ceres as a function of core radius. Typical values of grain density[13] are shown for H-chondrite (black circle), unaltered carbonaceous chondrite (CO or CV chondrites; green circle), moderately to extensively altered CM chondrite (blue circle) and pervasively altered CI chondrite (red circle). A band of ±100 kg m^{-3} is shown for the latter two examples to take account of potential variability in density within a given group. Assuming that the interior of Ceres is made up of CM-class chondrites (that is, 2,900 kg m^{-3}) yields a core size estimate of about 280 km and a mean outer shell of thickness about 190 km and a density of about 1,950 kg m^{-3}. Assuming that the interior of Ceres is made up of highly altered CI-class chondrites (that is, 2,460 kg m^{-3}) yields a core size estimate of about 400 km and a mean outer-shell thickness of about 70 km and a density of about 1,680 kg m^{-3}.

in the shell thickness, with a strong outer shell that has retained its geometry over geologic timescales, as discussed in more detail below.

Two-way X-band (8.4 GHz) radiometric range and Doppler tracking measurement of the Dawn spacecraft were also acquired and processed to obtain the gravity field[7]. This yields in an estimated mass of $M = (938.416 \pm 0.013) \times 10^{18}$ kg. Combining the mass and volume values gives the bulk density of 2,162 ± 8 kg m^{-3}. That density is <5% greater than inferred previously[2] owing to updated and more accurate shape data. As shown in previous studies[1,4], the density of Ceres is much less than that of a typical rocky body, such as the Moon or Vesta (~3,300–3,500 kg m^{-3}), indicating a mixture of volatiles and rocky materials.

Gravity science observations also yield a degree-8 gravity field[7] (Extended Data Table 1), with coefficients determined with sufficient accuracy up to degree 5 (that is, the magnitude spectrum of uncertainty is lower than the estimated magnitude spectrum), which gives a half-wavelength resolution of about 300 km (Fig. 2). The measured second-degree, first-order gravity coefficients[7]—that is, C_{21} and S_{21}—are small compared to the other degree-2 coefficients, indicating that Ceres is rotating very nearly about the principal axis of the greatest inertia, with no measurable wobble[18], implying no recent excitation[19] (Extended Data Table 1). This suggests that the orbit of Ceres must have been free from substantial impact for many hundreds of thousands of years, as expected for an object the size of Ceres, given that it would take an enormous amount of energy to create a wobble that would be measurable using Dawn's image data.

In addition, the degree-2 gravity harmonics are dominated by the zonal term J_2, which is driven by rotational flattening. As Ceres has no significant tides, the main force acting to produce departures from spherical symmetry is rotation, and if Ceres were in hydrostatic equilibrium, then the only departures from spherical symmetry would be in the form of a zonal flattening. That is, all degree-2 spherical harmonics, except for J_2, should be zero. Following this logic, the measured hydrostaticity matches that predicted within an error of 3%. This hydrostaticity is also supported by the degree-2 and -4 coefficients of the Ceres gravity field, where their magnitude spectra are dominated by the zonal (that is, latitudinally dependent) components, indicating that the gravity field has an almost ellipsoidal shape (Fig. 2 and Extended Data Table 1).

In contrast to Vesta, different internal processes are at work on Ceres. Whereas the gravity on Vesta is mainly determined by the topography on the surface, the gravity of Ceres is noticeably suppressed when compared to the signal predicted by the topography (Fig. 2). The Bouguer anomaly map (that is, observed gravity minus the gravity from homogeneous Ceres with mean density) shows that low values correlate with the high-topography areas, and vice versa, indicating an isostatic compensation of the surface of Ceres (Fig. 1a and b). The presence of topographic features at all scales[20,21] indicates the presence of a strong outer shell, while compensation points to a decrease of viscosity at depth that is probably thermally controlled[1,4]. Salts have also been suggested as second-phase impurities that could weaken the subsurface and produce a few per cent melt, consistent with the emplacement of the mountain on Ceres called Ahuna Mons[22].

The larger value of the degree-2 zonal harmonic calculated assuming a homogeneous Ceres with mean density, as compared to the observed J_2 is most easily (but non-uniquely) interpreted as evidence for a density gradient, with lower-density material near the surface. A first step towards interpreting these data are to assume a two-layer structure, that is, a core and a shell. By invoking the Radau–Darwin approximation[10,23,24], based on the observed degree-2 gravity coefficients together with the assumption of hydrostatic equilibrium, we compute the normalized mean moment of inertia of Ceres of 0.37, which is large compared to those of the bodies expected to have experienced full differentiation, such as Ganymede (~0.31)[25], and is more comparable to those of Titan (~0.34)[26] and Callisto (~0.36)[25]. The latter two

are believed to maintain large non-hydrostatic anomalies that could mask actual information on their density profiles[27]. However, Ceres is a fast rotator and its moment of inertia is less affected by non-hydrostatic anomalies[27], so the derived moment of inertia is expected to be representative of the interior of Ceres. Therefore, the magnitude of J_2, combined with the hydrostatic assumption, does reflect a central mass concentration. With these assumptions, we estimate the density and thickness of the inner and outer layers of Ceres from the observations by numerically integrating Clairaut's equations of rotational equilibrium to third order[9]. These approaches yield a family of solutions for core radius versus core density (Fig. 3). If the radial density variations are monotonic, then the actual density profile must fall within the envelope provided by the core and shell density curves (Fig. 3). The numerical solution, coupled with the assumption that the shell density cannot be less than 930 kg m^{-3} (that is, pure water ice), indicates that the density of the inner core cannot be less than about 2,400 kg m^{-3}. This value is slightly lower than the grain density (that is, the zero-porosity density value) inferred for the most altered (and least dense) carbonaceous chondrites[13], that is, 2,460 kg m^{-3}, which yields an outer-shell thickness of about 70 km and density of about 1,680 kg m^{-3} (Fig. 3).

Ceres, however, is large enough that carbonaceous chondrite material would undergo some thermal metamorphism at depth[1,4], accompanied by the migration of salt species upon mild heating[5]. Advanced metamorphism, a scenario that would imply an early time of formation involving a substantial amount of ^{26}Al, would partially dehydrate the core material of Ceres, driving off some of the volatiles and increasing the core density. On the other hand, incomplete aqueous alteration of the original igneous minerals may also lead to relatively higher core densities. Assuming that the density of Ceres' deep interior may be approximated by that of CM chondrites[13] (that is, a grain density of 2,900 kg m^{-3}), which have undergone advanced aqueous alteration, the numerical solution leads to a core size estimate of approximately 280 km. This corresponds to a mean outer-shell thickness of 190 km and a density of about 1,950 kg m^{-3} (Fig. 3). The high shell density may reflect the redistribution of elements from the rock to the volatile phase as a consequence of aqueous alteration, enriching the shell in salt compounds[4,9,28] or it may reflect an enrichment of the outer shell in silicate material, as in the muddy mantle model[6], or both. The potential enrichment of Ceres' shell in salts is further supported by the direct detection of sodium bicarbonate and ammonium compounds at the Occator crater on Ceres[14] as well as geological observations[21]. The modelled shell density reaches a maximum of 1,970 kg m^{-3} for a fully anhydrous core (3,500 kg m^{-3}). However, full dehydration of the core is not expected, on the basis of thermal models[4,6].

Overall, the geophysical observations acquired by the Dawn spacecraft, and inferred constraints, demonstrate that Ceres has undergone physical and chemical differentiation. This is consistent with the observed surface mineralogy suggesting that Ceres went through a phase of aqueous alteration[14] following the melting of its volatile phase. These results resolve an enduring uncertainty on the nature of Ceres' interior concerning the relative likelihood of the undifferentiated[3] and fully differentiated models[4]—both of which can now be ruled out. The departure from a fully differentiated interior reflects the role of water in moderating thermal evolution, as well as formation after several half-lives of ^{26}Al. This contrasts with Vesta, which accreted earlier, lost most of its water and experienced substantial internal differentiation[29]. The internal structure of Ceres presented here, combined with other Dawn observations[14,20–22,30], will help to constrain Ceres' physical and chemical evolution, and provide critical insight into the differentiation of other large ice-rich rocky bodies.

Online Content Methods, along with any additional Extended Data display items and Source Data, are available in the online version of the paper; references unique to these sections appear only in the online paper.

Received 9 February; accepted 27 May 2016.
Published online 3 August 2016.

1. McCord, T. B. & Sotin, C. Ceres: evolution and current state. *Geophys. Res. Lett.* **110,** E05009 (2005).
2. Thomas, P. C. *et al.* Differentiation of the asteroid Ceres as revealed by its shape. *Nature* **437,** 224–226 (2005).
3. Zolotov, M. Y. On the composition and differentiation of Ceres. *Icarus* **204,** 183–193 (2009).
4. Castillo-Rogez, J. C. & McCord, T. B. Ceres' evolution and present state constrained by shape data. *Icarus* **205,** 443–459 (2010).
5. Castillo-Rogez, J. C. Ceres—neither a porous nor salty ball. *Icarus* **215,** 599–602 (2011).
6. Neveu, M. & Desch, S. J. Geochemistry, thermal evolution, and cryovolcanism on Ceres with a muddy ice mantle. *Geophys. Res. Lett.* **42,** 10,197–10,206 (2015).
7. Heiskanen, W. A. & Moritz, H. *Physical Geodesy* (W. H. Freeman and Company, 1967).
8. Konopliv, A. S. *et al.* The Vesta gravity field, spin pole and rotation period, landmark positions, and ephemeris from the Dawn tracking and optical data. *Icarus* **240,** 103–117 (2014).
9. Rambaux, N. *et al.* Third-order development of shape, gravity, and moment of inertia for highly celestial bodies. Application to Ceres. *Astron. Astrophys.* **584,** A127 (2015).
10. Anderson, J. D. *et al.* Gravitational constraints on the internal structure of Ganymede. *Nature* **384,** 541–543 (1996).
11. Kucinskas, A. B. & Turcotte, D. L. Isostatic compensation of equatorial highlands on Venus. *Icarus* **112,** 104–116 (1994).
12. Bills, B. G. *et al.* Harmonic and statistical analyses of the gravity and topography of Vesta. *Icarus* **240,** 161–173 (2014).
13. Consolmagno, G. J. *et al.* The significance of meteorite density and porosity. *Chem. Erde* **68,** 1–29 (2008).
14. De Sanctis, M. C. *et al.* Ammoniated phyllosilicates with a likely outer Solar System origin on (1) Ceres. *Nature* **528,** 241–244 (2015).
15. Russell, C. T. *et al.* Dawn arrives at Ceres: exploration of a small volatile-rich world. *Science* (in the press).
16. Gaskell, R. W. *et al.* Characterizing and navigating small bodies with imaging data. *Meteorit. Planet. Sci.* **43,** 1049–1061 (2008).
17. Preusker, F. *et al.* Shape model, reference system definition, and cartographic mapping standards for comet 67P/Churyumov-Gerasimenko—stereo-photogrammetric analysis of Rosetta/OSIRIS image data. *Astron. Astrophys.* **583,** A33 (2015).
18. Peale, S. J. Excitation and relaxation of the wobble, precession, and libration of the Moon. *J. Geophys. Res.* **81,** 1813–1827 (1976).
19. Rambaux, N. *et al.* Constraining Ceres' interior from its rotational motion. *Astron. Astrophys.* **535,** A43 (2011).
20. Buczkowski, D. *et al.* The geomorphology of Ceres. *Science* (in the press).
21. Hiesinger, H. *et al.* Cratering on Ceres: implications for its crust and evolution. *Science* (in the press).
22. Ruesch, O. *et al.* Cryovolcanism on Ceres. *Science* (in the press).
23. Radau, R. Sur la loi des densités a l'intérieur de la Terre. *Compt. Rend.* **100,** 972–974 (1885).
24. Darwin, G. H. The theory of the figure of the Earth carried to the second order of small quantities. *Mon. Not. R. Astron. Soc.* **60,** 82–124 (1900).
25. Showman, A. P. & Malhotra, R. The Galilean satellites. *Science* **286,** 77–84 (1999).
26. Iess, L. *et al.* Gravity field, shape, and moment of inertia of Titan. *Science* **327,** 1367–1369 (2010).
27. Gao, Pa & Stevenson, D. J. Nonhydrostatic effects and the determination of icy satellite moments of inertia. *Icarus* **226,** 1185–1191 (2013).
28. Kargel, J. S. *et al.* Europa's crust and ocean: origin, composition, and the prospects for life. *Icarus* **148,** 226–265 (2000).
29. Castillo-Rogez, J. C. & Young, E. Origin and evolution of volatile-rich asteroids. In *Planetesimals: Early Differentiation and Consequences for Planets* (eds Elkins-Tanton, L. & Weiss, B.) Ch. 4 (Cambridge Univ. Press, in the press).
30. Nathues, A. *et al.* Sublimation in bright spots on (1) Ceres. *Nature* **528,** 237–240 (2015).

Acknowledgements This research was carried out in part at the Jet Propulsion Laboratory, California Institute of Technology, under a contract with the National Aeronautics and Space Administration. We thank the Dawn operations team for the development, cruise, orbital insertion and operations of the Dawn spacecraft at Ceres. R.S.P. thanks W. M. Folkner, E. M. Mazarico, and M. D. Rayman for comments and suggestions. N.R. is grateful to the CNU, Section 34, for supporting a six-month full-time research project through CRCT-2015 funding delivered by the MESR and acknowledges funding from the French National Programme of Planetology (PNP). M.J.T. acknowledges funding by the CNES. Government sponsorship acknowledged. All rights reserved.

Author Contributions R.S.P., A.S.K. and A.T.V. performed data analysis and calibration. R.S.P., B.G.B., N.R., J.C.C.-R., C.A.R., A.I.E., M.T.Z., R.R.F., M.J.T., C.T.R., A.N. and F.P. contributed to the interpretation of the data. All authors contributed to the discussion of the results and to writing the paper.

Author Information The gravity science and framing camera data is available through the PDS Small Bodies Node website (http://sbn.pds.nasa.gov/data_sb/missions/dawn). Reprints and permissions information is available at www.nature.com/reprints. The authors declare no competing financial interests. Readers are welcome to comment on the online version of the paper. Correspondence and requests for materials should be addressed to R.S.P. (Ryan.S.Park@jpl.nasa.gov).

METHODS

Data set from the Dawn mission. The data arc considered in this study starts on 4 February 2015, just after the time when the Framing Camera (FC) image resolution exceeded that of the Hubble Space Telescope, and ends on 24 October 2015, which is the end of the High-Altitude Mapping Orbit (HAMO) phase. The orbit radius for each phase is about 14,000 km (Approach), 4,860 km (Survey), and 1,940 km (HAMO). Although the best image and gravity data come from the HAMO phase (that is, the lowest altitude considered in this study), higher-altitude data are also used since they are helpful for determining long-wavelength features.

The Dawn spacecraft is equipped with a primary and a back-up framing camera with image resolution of 93 μrad per pixel[30]; the FC2 camera (primary) was used during the data arc considered here. A total of about 4,300 images were taken during this period with image resolution in the range 0.14–7.79 km per pixel. The camera bore-sight almost always points to nadir, and thus, the image resolution strictly depends on the altitude; however, we note that the incidence angle (that is, the angle between the camera bore-sight and the Sun direction) is also important for shape determination[16,17].

The Dawn telecom subsystem is capable of X-band (8.4 GHz) uplink and downlink compatible with NASA's Deep Space Network stations for the gravity science investigation. The range and Doppler data acquired by the Dawn spacecraft measure the distance and line-of-sight velocity of Dawn relative to a Deep Space Network station, respectively. The radio tracking was continuous except for when Dawn was thrusting to lower its orbit. There were no ion-thrust interruptions during the Survey and HAMO phases.

The radio data and landmarks derived using the stereo-photoclinometry technique are then processed to determine global parameters of Ceres through an orbit determination process[11]. The root-mean-square residuals of the processed range, Doppler, and imaging data were 0.5 m, 0.02 mm s^{-1} (60 s integration time), and 0.2 pixels, respectively.

Ceres shape determination. An accurate shape model is crucial for understanding the geophysical nature of Ceres. Using the images acquired during the science phases, a stereo-photoclinometry method was applied to construct a three-dimensional shape model of Ceres. The stereo-photoclinometry technique is different from a conventional stereo method in the sense that stereo uses parallax in overlapping images and photoclinometry estimates slopes from changes in brightness with variations in illumination and view angles, allowing construction of high-resolution topography and albedo maps[16].

First, an a priori shape model is gridded with overlapping maps. For each map, a set of images with visibility of the map location is extracted, ortho-rectified and projected onto the a priori shape model. Each image was evaluated before inclusion in the model. Saturated images were discarded, in particular the over-exposed images acquired by the navigation team for the purpose of a star-based pointing solution. Images with high phase angles were not dismissed out of hand, but were evaluated in the model and later discarded if they consistently failed to register with any maps, especially with higher-resolution maps that were created later. Registration outliers between image data and existing maps were addressed individually, and very little data was deleted (<1%). Registration errors were adjusted by hand to provide a better a priori location for the automated process. Occasionally, it was necessary to reduce the allowable ratio of image resolution to map resolution to prevent older, lower-resolution images from softening the map.

Once all images are registered, a brightness model for each image is constructed based on a reflectance function, slope and local geometry, and solar and camera geometry. Note that the reflectance model used in this study is the same model used for the Vesta phase of the mission. This model is phase-dependent and has produced map renders that are visually similar to the source image data. A least-squares fit is then made between each brightness model and its projected image to estimate the local slope and relative albedo. Finally, the topographic slopes are integrated to construct local heights and all maps are combined to produce a global shape. The centre of each map is often called a landmark or a control point. Since landmarks are fixed points relative to Ceres, landmarks in an image can be used to triangulate the position of Dawn.

The main error sources for stereo-photoclinometry are the uncertainties in the spacecraft position and camera pointing direction, which are difficult to separate. This is mainly because the image data alone are not sensitive enough to determine the radial position of the camera. Also, it is difficult to identify systematic errors in the long-wavelength topographic variation when combining maps to create a global three-dimensional shape. We resolve these errors by combining the optical data with radio data to better constrain the spacecraft and landmark positions through an orbit determination process. The Doppler data measure the line-of-sight velocity of Dawn relative to a Deep Space Network station extremely accurately, which is very sensitive to the radial distance, especially for low altitudes. Overall, shape determination is an iterative process of stereo-photoclinometry and orbit determination until the solution converges, and we note that it is crucial to combine both processes to minimize potential systematic errors.

Given a three-dimensional shape, it is often helpful to determine a best-fit ellipsoid for various geophysical interpretations. We first note that the shape model we determine is with respect to the centre of mass, and there are several different ways for computing a best-fit ellipsoid (Extended Data Table 2). The best fitting method for geophysical interpretation is where we estimate nine parameters, that is, three semi-principal axes (a_e, b_e and c_e), the orientation angles of the three principal axes (θ_e, ϕ_e and ψ_e), and the three-dimensional centre of ellipsoid (c_x, c_y and c_z). Note that the orientation angles and the Cartesian centre of ellipsoid are defined with respect to the Ceres body-fixed frame, which is co-aligned with the frame where the gravity field is determined. The unit vectors along the three principal axes are defined as:

$$\boldsymbol{u}_a = \begin{bmatrix} +\cos\theta_e\sin\phi_e\cos\psi_e - \sin\theta_e\sin\psi_e \\ +\sin\theta_e\sin\phi_e\cos\psi_e + \cos\theta_e\sin\psi_e \\ -\cos\phi_e\cos\psi_e \end{bmatrix}$$

$$\boldsymbol{u}_b = \begin{bmatrix} -\cos\theta_e\sin\phi_e\sin\psi_e - \sin\theta_e\cos\psi_e \\ -\sin\theta_e\sin\phi_e\sin\psi_e + \cos\theta_e\cos\psi_e \\ +\cos\phi_e\sin\psi_e \end{bmatrix}$$

$$\boldsymbol{u}_c = \begin{bmatrix} +\cos\theta_e\cos\phi_e \\ +\sin\theta_e\cos\phi_e \\ +\sin\phi_e \end{bmatrix}$$

The best-fitting method results in the principal semi-axes of (483.1 km, 481.0 km, 445.9 km), which gives a polar flattening of $[(a+b)/2 - c]/[(a+b)/2] = 0.075$, with the ellipsoid major axis along the (47.4° E, 0.1° S) direction (Fig. 1a).

Another useful definition of a best-fitting ellipsoid is where the principal axes directions are fixed with respect to the Ceres body-fixed frame and only the principal axes and ellipsoid centre are computed (Extended Data Table 2). The resulting principal semi-axes are (482.0 km, 482.1 km, 445.9 km), which we approximate as (482 km, 482 km, 446 km). We call this case the mean reference ellipsoid and used it to make Mollweide projections of topography and the Bouguer anomaly (Fig. 1a and b). In both cases, the mean volumetric radius is about 470 km, and both show that Ceres' shape is almost spheroidal (that is, $a_e \approx b_e$).

Ceres gravity and rotation determination. The external gravitational potential of Ceres that attracts the motion of the Dawn spacecraft can be modelled using a spherical harmonic expansion[7]:

$$U(r,\lambda,\phi) = \frac{GM}{r}\sum_{n=0}^{\infty}\sum_{m=0}^{n}\left(\frac{R}{r}\right)^n P_{nm}(\sin\phi)[C_{nm}\cos(m\lambda) + S_{nm}\sin(m\lambda)]$$

where G is the universal gravitational constant, M is the mass of Ceres, R is the reference radius of Ceres (470 km), P_{nm} are the associated Legendre functions, and C_{nm} and S_{nm} are the un-normalized spherical harmonic coefficients (the corresponding un-normalized zonal harmonics are $J_n = -C_{n0}$). The un-normalized spherical harmonic coefficients are related to the normalized spherical harmonic coefficients as follows: $(\bar{C}_{nm}, \bar{S}_{nm})N_{nm} = (C_{nm}, S_{nm})$, where the normalization factor N_{nm} is defined as:

$$N_{nm} = \sqrt{\frac{(2-\delta_{0m})(2n+1)(n-m)!}{(n+m)!}}$$

Here, δ_{0m} represents the Kronecker delta function. For degree-2 coefficients, the normalization factors are $N_{20} = \sqrt{5}$, $N_{21} = \sqrt{5/3}$, and $N_{22} = \sqrt{5/12}$. The gravitational acceleration of an external point mass—defined by the latitude ϕ, longitude λ and radius r—is given by the gradient of this potential. Since the gravity field of Ceres perturbs Dawn's orbit, both gravity field and rotational parameters can be estimated by accurately tracking the spacecraft motion.

The gravity field is modelled in a Ceres body-fixed frame, and its inertial orientation in the International Celestial Reference Frame is modelled using $\{\alpha, \delta, W_0 + \Omega\Delta t\}$, where α represents the spin-pole right ascension, δ represents the spin-pole declination, W_0 represents the prime-meridian angle (170.65°), Ω represents the rotation rate, and Δt represents the time elapsed since J2000. The resulting estimates give the pole right ascension, $\alpha_0 = (291.421 \pm 0.007)°$, and pole declination, $\delta_0 = (66.758 \pm 0.002)°$. Note that W_0 was chosen such that the small crater on Ceres named Kait defines the 0° longitude position, which is not aligned with the principal axes frame defined by the gravity field. The accuracy of the rotation rate estimate, based on the data acquired up to the 1,940-km-radius

mapping orbit, is comparable to the value obtained by light-curve analysis[2], that is, $\Omega = (952.1532 \pm 0.0001)°$ per day.

Moment of inertia from the Radau–Darwin relation. The degree-2 gravity coefficients provide five constraints on the moments and products of inertia of the body[7]:

$$J_2 MR^2 = I_{33} - (I_{11} + I_{22})/2$$

$$C_{21} MR^2 = I_{13} = I_{31}$$

$$S_{21} MR^2 = I_{23} = I_{32}$$

$$C_{22} MR^2 = (I_{22} - I_{11})/4$$

$$S_{22} MR^2 = I_{12}/2 = I_{21}/2$$

If Ceres were in a state of principal axis rotation, the product of the inertia terms I_{13} and I_{23} would be zero, and this would yield $C_{21} = S_{21} = 0$. From the results in Extended Data Table 1, the principal-axis rotation of Ceres is nearly confirmed. We note that it is possible to find a principal-axis coordinate system in which $C_{21} = S_{21} = S_{22} = 0$ is satisfied. From the observed gravity field, the principal semi-axes directions are $p_1 = \{-24° \text{ E}, 0° \text{ N}\}$, $p_2 = \{66° \text{ E}, 0° \text{ N}\}$, and $p_3 = \{0° \text{ E}, 90° \text{ N}\}$, so that the only non-zero coefficients would be $J_2 = 264.99 \times 10^{-4}$ and $C_{21} = 2.383 \times 10^{-4}$.

The dimensional form of the rotational potential can be written as $\Phi_{\text{rot}} = \frac{1}{2}\Omega^2 R^2 \cos^2\phi$. The non-dimensional, degree-2 component of this potential is $q = \frac{\Omega^2 R^3}{GM}$, and the corresponding hydrostatic flattening is $J_2(R/R_{\text{eq}}) = \lambda q$, where $R_{\text{eq}} \approx 482$ km represents the mean equatorial radius and λ is a dimensionless scale factor. We measure the hydrostaticity of Ceres by computing a ratio between non-zonal degree 2 coefficients and J_2 (that is, $\sqrt{\bar{C}_{22}^2 + \bar{S}_{22}^2}/\bar{J}_2$), which yields an error of about 3% and it would be reasonable to assume that Ceres is in hydrostatic equilibrium. For a body in hydrostatic equilibrium, the only force resisting tidal or rotational deformation is the body's own gravity, which depends upon the radial density profile. The Radau–Darwin relation yields an explicit relationship between λ and the polar moment of inertia, and hence provides an additional constraint for the full moment of inertia[23,24].

If we denote the principal moments of inertia as $I_{11} < I_{22} < I_{33}$, where I_{33} represents the polar moment of inertia, and their dimensionless counterparts as:

$$\begin{bmatrix} a \\ b \\ c \end{bmatrix} = \frac{1}{MR^2} \begin{bmatrix} I_{11} \\ I_{22} \\ I_{33} \end{bmatrix}$$

then we can write the Radau–Darwin relation scaled to the volumetric radius R as[27]:

$$c = \frac{2}{3}\left(\frac{R_{\text{eq}}}{R}\right)^2 \left(1 - \frac{2}{5}\sqrt{\frac{5}{3\lambda + 1} - 1}\right)$$

Solving for the dimensionless scale factor $\lambda = 0.41$ and applying it to the above Radau–Darwin relation yields the dimensionless polar moment of inertia as $c = 0.39$. If we ignore the small C_{21} and S_{21} terms, the remaining principal moments of inertia can be approximated as:

$$\begin{bmatrix} a \\ b \end{bmatrix} = (c - J_2)\begin{bmatrix} 1 \\ 1 \end{bmatrix} + \sqrt{C_{22}^2 + S_{22}^2}\begin{bmatrix} -2 \\ +2 \end{bmatrix}$$

From this relation, we get the remaining constraint for solving for the full moment of inertia matrix in the form of the mean moment of inertia $I = (I_{11} + I_{22} + I_{33})/3 = 0.37MR^2$.

The recovered value differs from that of a uniform-density sphere, which has a dimensionless polar moment value of $c = 0.4$. The resulting principal moments of inertia are $I_{11} = 0.36MR^2$, $I_{22} = 0.36MR^2$ and $I_{33} = 0.39MR^2$, and the products of inertia (that is, I_{12}, I_{13} and I_{23}) are effectively zero. Considering that Ceres has a relatively high polar flattening, the mean moment of inertia would be a better representative of its average interior structure. Thus, we use the mean moment of inertia of Ceres when comparing its level of mass concentration instead of the polar moment of inertia which was used to represent the interior of Ganymede, Titan and Callisto[25,26].

Numerical solutions of hydrostatic equilibrium assumptions. We investigated a model of a two-layer Ceres interior based on forward modelling and the assumption that Ceres is in hydrostatic equilibrium. In this method, the ellipsoidal shape (a_{h}, b_{h} and c_{h}) and the gravity coefficient J_2^{h} are computed for a two-layer model under the assumption of hydrostatic equilibrium. To reach an accuracy of tens of metres, it is necessary to solve numerically the Clairaut's equations of rotational equilibrium at third order[9]. We apply a third-order model[9] to a grid of interior models, varying the core density between the bulk density and 4,000 kg m^{-3} and the core radius between 190 km and 470 km (Extended Data Fig. 1). For comparison, the solutions coming from an alternative approach[27] are also superimposed (Extended Data Fig. 1).

Code availability. We have opted not to make the code available because it is based on well-known theories for orbit and shape determinations, as described in Methods.

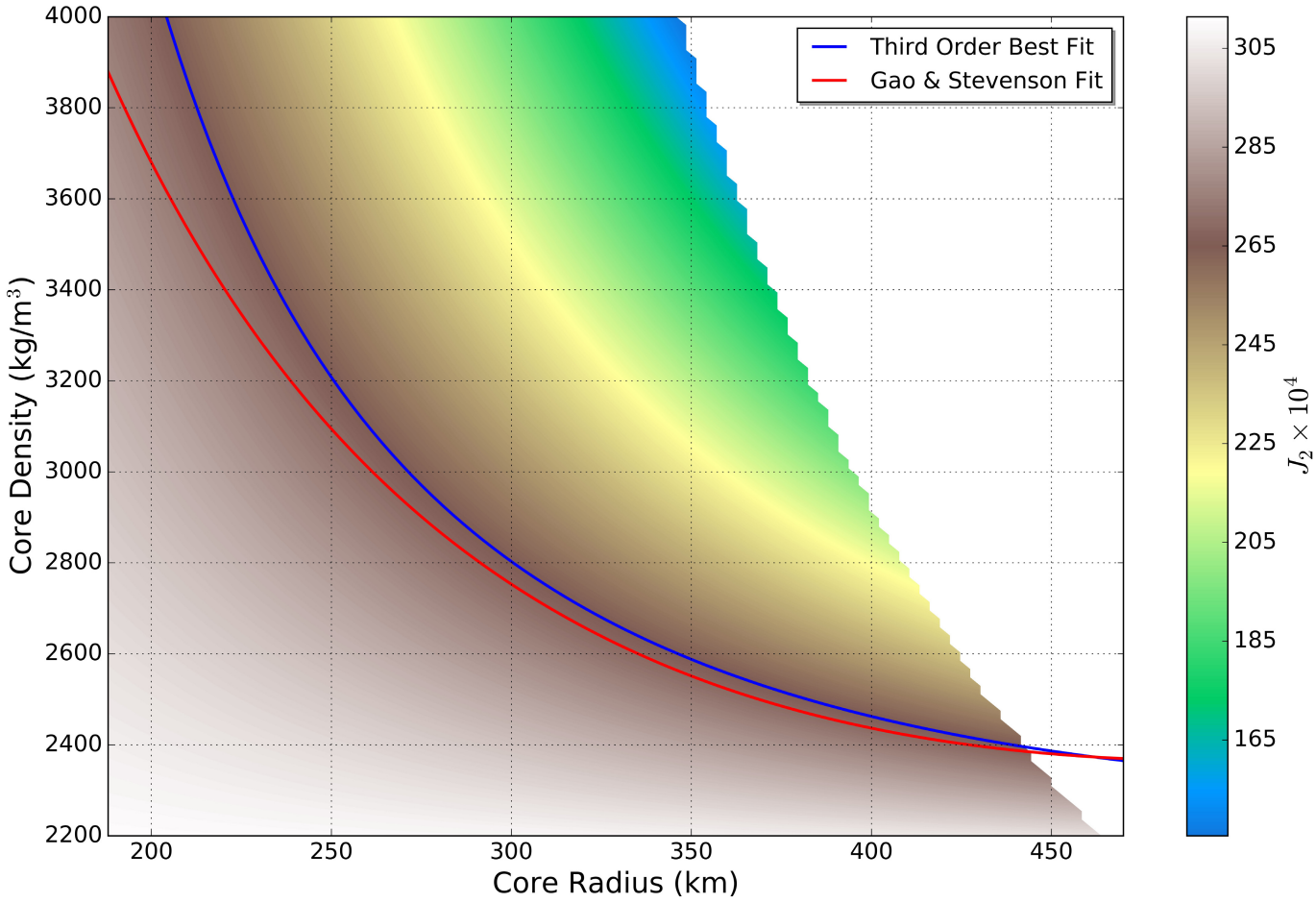

Extended Data Figure 1 | Range of values for the degree-2 zonal gravity coefficient for Ceres. We assume a two-layer model for Ceres and vary the density and radius of the core by solving Clairaut's equations of rotational equilibrium at third order[9]. The best-fitting solution for $J_2 = 264.99 \times 10^{-4}$ (blue line) is compared with the direct approach of Gao and Stevenson[27] (red line), which generally shows a good agreement except at high core-density values. The white area at the upper right corresponds to solutions with shell density below 900 kg m^{-3}.

Extended Data Table 1 | Gravity spherical harmonic coefficients of Ceres[7]

Degree n	Order m	Estimated spherical harmonics, $J_n = -C_{n0}$, with $R = 470\ \mathrm{km}$, $GM = 62.6284 \pm 0.0009\ \mathrm{km^3/s^2}$		Uncertainty of estimated spherical harmonics		Spherical harmonics derived assuming a homogeneous Ceres, $J_n^* = -C_{nm}^*$	
		C_{nm}	S_{nm}	$\sigma_{C_{nm}}$	$\sigma_{S_{nm}}$	C_{nm}^*	S_{nm}^*
1	0	0.0000e+00	-	0.0e+00	-	8.59e-04	-
1	1	0.0000e+00	0.0000e+00	0.0e+00	0.0e+00	-1.76e-03	-7.54e-04
2	0	-2.6499e-02	-	8.4e-07	-	-3.04e-02	-
2	1	-1.0773e-07	9.0669e-08	3.6e-07	3.6e-07	2.47e-04	-3.02e-04
2	2	1.5960e-04	-1.7698e-04	2.4e-07	2.4e-07	-2.35e-05	4.60e-04
3	0	1.0669e-04	-	1.5e-06	-	3.46e-04	-
3	1	2.5224e-05	6.7279e-05	9.8e-07	9.8e-07	2.04e-04	6.12e-05
3	2	-6.6830e-06	2.4152e-05	3.6e-07	3.6e-07	-4.33e-05	1.35e-04
3	3	-6.8203e-06	-1.2523e-05	1.3e-07	1.3e-07	-1.01e-05	-5.25e-06
4	0	1.7124e-03	-	5.5e-06	-	2.14e-03	-
4	1	-2.2337e-05	-2.3315e-06	2.6e-06	2.6e-06	-5.17e-06	1.32e-04
4	2	3.5842e-06	-3.7586e-06	7.7e-07	7.7e-07	2.95e-06	-3.82e-05
4	3	-1.4449e-06	-1.9433e-07	2.5e-07	2.5e-07	-4.79e-06	-1.29e-06
4	4	5.7393e-07	5.8739e-07	6.7e-08	6.8e-08	1.83e-06	-6.74e-07
5	0	-4.2767e-06	-	2.3e-05	-	-2.31e-05	-
5	1	1.2753e-05	-1.8690e-05	6.2e-06	6.0e-06	8.82e-06	-4.02e-05
5	2	-2.2163e-06	1.5386e-07	2.2e-06	2.2e-06	-1.86e-05	-2.75e-06
5	3	8.9730e-07	-1.0415e-06	4.7e-07	4.7e-07	7.00e-07	-1.84e-06
5	4	-2.6860e-07	1.9510e-07	8.8e-08	9.0e-08	-1.18e-06	4.36e-08
5	5	-5.8186e-08	4.7974e-08	3.0e-08	3.0e-08	-2.61e-07	1.16e-07
6	0	-1.0585e-04	-	9.3e-05	-	5.76e-05	-
6	1	7.9961e-06	2.7243e-05	2.0e-05	2.0e-05	-9.84e-06	-3.66e-06
6	2	-7.3674e-08	4.8924e-08	5.5e-06	5.4e-06	2.06e-06	2.36e-06
6	3	-1.0968e-07	8.8478e-07	1.0e-06	1.0e-06	1.97e-07	2.32e-06
6	4	1.3375e-07	-7.3491e-08	2.1e-07	2.1e-07	1.60e-07	-1.09e-07
6	5	2.7038e-08	1.8979e-08	3.3e-08	3.2e-08	5.13e-08	2.04e-08
6	6	-2.9569e-09	-1.8315e-09	1.2e-08	1.2e-08	-2.83e-09	-1.15e-08
7	0	3.4269e-04	-	3.4e-04	-	3.33e-05	-
7	1	1.1373e-05	1.9928e-05	6.8e-05	6.9e-05	-5.00e-06	3.03e-06
7	2	2.3881e-06	1.1584e-06	1.1e-05	1.1e-05	6.19e-06	-5.29e-07
7	3	-4.0956e-07	-1.0485e-06	2.7e-06	2.7e-06	-5.70e-07	-1.08e-07
7	4	-6.7759e-09	-1.6810e-07	4.5e-07	4.5e-07	1.10e-07	-8.80e-08
7	5	-2.0116e-08	-1.5094e-08	5.2e-08	5.2e-08	6.12e-09	-2.00e-08
7	6	1.2636e-09	4.6201e-09	1.1e-08	1.1e-08	-1.97e-10	-4.80e-10
7	7	7.9531e-11	-5.9061e-10	3.7e-09	3.8e-09	1.70e-10	-1.05e-09
8	0	5.4935e-04	-	1.3e-03	-	8.32e-05	-
8	1	9.7461e-05	1.4256e-04	2.3e-04	2.3e-04	-4.02e-06	8.53e-06
8	2	4.6832e-06	-7.6807e-06	2.9e-05	2.9e-05	-3.47e-06	8.98e-07
8	3	1.0859e-07	6.4252e-07	5.6e-06	5.6e-06	-3.73e-07	-3.71e-08
8	4	1.9677e-07	3.5067e-09	7.6e-07	7.6e-07	-4.96e-09	3.16e-08
8	5	-1.1208e-09	-4.0262e-08	9.5e-08	9.7e-08	3.97e-09	-4.13e-12
8	6	-2.5037e-09	2.6829e-09	1.4e-08	1.4e-08	3.86e-10	-1.11e-09
8	7	-1.3957e-10	6.6921e-11	2.8e-09	2.8e-09	-1.34e-10	1.84e-10
8	8	-3.1041e-11	4.2805e-11	7.9e-10	7.9e-10	6.24e-11	3.33e-11

The observed un-normalized coefficients C_{nm} and S_{nm} up to degree and order 8 (named CERES08A) are computed from Dawn's tracking data. The parameters $\sigma_{C_{nm}}$ and $\sigma_{S_{nm}}$ represent the uncertainties of C_{nm} and S_{nm}, which are computed by multiplying the formal standard deviations by a factor of six to account for potential systematic errors. The last two columns show the un-normalized spherical harmonic coefficients derived from topography assuming a homogeneous Ceres with mean density, denoted with an asterisk.

Extended Data Table 2 | Various best-fitting ellipsoid estimates of the shape of Ceres with respect to the centre of mass

Cases	a_e (km)	b_e (km)	c_e (km)	θ_e (deg)	ϕ_e (deg)	ψ_e (deg)	c_x (km)	c_y (km)	c_z (km)	RMS_e (km)
Ellipsoid with orientation and centre	483.1	481.0	445.9	307.58	90.80	99.84	-0.87	-0.34	0.41	1.64
Ellipsoid with centre	482.0	482.1	445.9	0.00	90.00	0.00	-0.87	-0.34	0.41	1.74
Ellipsoid with orientation	483.1	481.0	445.9	307.55	90.79	99.87	0.00	0.00	0.00	1.74
Ellipsoid	482.0	482.1	445.9	0.00	90.00	0.00	0.00	0.00	0.00	1.83

Here, a_e, b_e and c_e represent the three principal semi-axes, θ_e, ϕ_e and ψ_e represent the orientation angles of the three principal axes, and c_x, c_y and c_z represent the three-dimensional Cartesian centre of the ellipsoid. Note that the orientation angles and the Cartesian centre of the ellipsoid are defined with respect to the Ceres body-fixed frame as defined by the gravity field. The first case shows the result by fitting all nine parameters, which is the best-fitting method for geophysical interpretation. The second case represents the mean reference ellipsoid, which was used for Mollweide projections (Fig. 1a and b). The RMS_e column shows the root-mean-square error of each fit, which shows that there is an improvement of about 100 m in estimating the orientation or the centre of the ellipsoid.